Journal of Materials Chemistry A

Accepted Manuscript

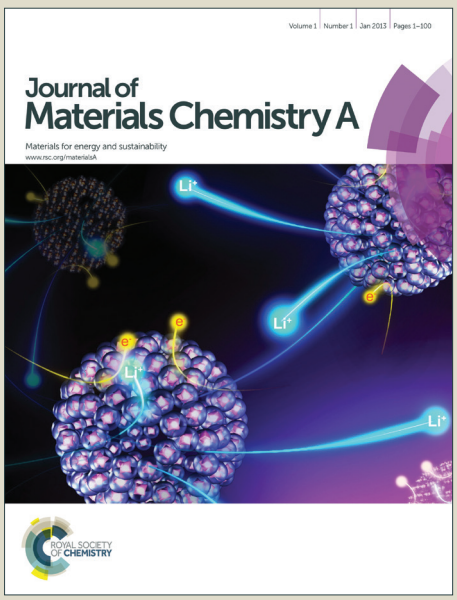

ROYAL SOCIETY OF CHEMISTRY

www.rsc.org/materialsA

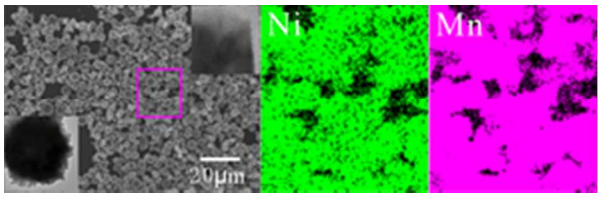

The micro-/nanostructured spherical intergrown $LiMn_2O_4$-$LiNi_{0.5}Mn_{1.5}O_4$ (LMO-LNMO I, $LiNi_{0.25}Mn_{1.75}O_4$) particles as a cathode material have been synthesized by an impregnation method with highly reactive chestnut-like MnO_2 nano-spheres as manganese source and structural template. The LMO-LNMO I is consisted of aggregates of nano-sized particles with a well-defined cubic spinel structure. The electrochemical performance and thermostability of LMO-LNMO I are better than that of the simple mechanical mixture of $LiMn_2O_4$ and $LiNi_{0.5}Mn_{1.5}O_4$ (LMO-LNMO M), and much better than that of $LiMn_2O_4$ and $LiNi_{0.5}Mn_{1.5}O_4$ monomer, individually. Within this special structure, LNMO acts as a skeleton to stabilize the structure of LMO, enables more lithium ions in LMO to participate in charge-discharge process along with these in LNMO, leading to high specific discharge capacities. In addition, this material exhibits excellent cycle stabilities at room temperature (25 ºC) as well as at elevated temperature. It presented a discharge capacity of 130 mAh•g−1, with 96.2% capacity retention after 100 cycles at 25 ºC at 1 C. When the temperature and rate are increased to 55 ºC and 5 C, it still delivers a discharge capacities of 131 mAh•g−1, with the capacity retention of 95% after 100 cycles. With the special impregnated synthetic methods, LMO-LNMO I shows a more homogeneous ion mixing at atomic level of Ni and Mn in the structure a more enhanced thermostability due to its high Mn content than LNMO. The structure stability and high electrical conductibility of LMO-LNMO I are responsible for the excellent electrochemical performance and outstanding thermal stability.

25x7mm (300 x 300 DPI)

Journal Name

RSCPublishing

ARTICLE

A Homogeneous Intergrown Material of $LiMn_2O_4$ and $LiNi_{0.5}Mn_{1.5}O_4$ as a Cathode Material for Lithium-Ion Batteries

Received 00th January 2012,
Accepted 00th January 2012

DOI: 10.1039/x0xx00000x

www.rsc.org/

Jing Wang, Yang-yang Yu, Bi-he Wu, Wei-qing Lin, Ji-yang Li and Jin-bao Zhao*

The micro-/nanostructured spherical intergrown $LiMn_2O_4$-$LiNi_{0.5}Mn_{1.5}O_4$ (LMO-LNMO I, $LiNi_{0.25}Mn_{1.75}O_4$) particles as a cathode material have been synthesized by an impregnation method with highly reactive chestnut-like MnO_2 nano-spheres as manganese source and structural template. The LMO-LNMO I is consisted of aggregates of nano-sized particles with a well-defined cubic spinel structure. The electrochemical performance and thermostability of LMO-LNMO I are better than that of the simple mechanical mixture of $LiMn_2O_4$ and $LiNi_{0.5}Mn_{1.5}O_4$ (LMO-LNMO M), and much better than that of $LiMn_2O_4$ and $LiNi_{0.5}Mn_{1.5}O_4$ monomer, individually. Within this special structure, LNMO acts as a skeleton to stabilize the structure of LMO, enables more lithium ions in LMO to participate in charge-discharge process along with these in LNMO, leading to high specific discharge capacities. In addition, this material exhibits excellent cycle stabilities at room temperature (25 ºC) as well as at elevated temperature. It presented a discharge capacity of 130 $mAh \cdot g^{-1}$, with 96.2% capacity retention after 100 cycles at 25 ºC at 1 C. When the temperature and rate are increased to 55 ºC and 5 C, it still delivers a discharge capacities of 131 $mAh \cdot g^{-1}$, with the capacity retention of 95% after 100 cycles. With the special impregnated synthetic methods, LMO-LNMO I shows a more homogeneous ion mixing at atomic level of Ni and Mn in the structure a more enhanced thermostability due to its high Mn content than LNMO. The structure stability and high electrical conductibility of LMO-LNMO I are responsible for the excellent electrochemical performance and outstanding thermal stability.

Introduction

The launching of environmental benign electric vehicle (EV), hybrid electric vehicle (HEV) and plug-in hybrid electric vehicle (PHEV) has accelerated rapid developments in the power battery technology and market.[1-5] As a new generation of high-energy battery, lithium ion batteries have many advantages such as high voltage, high specific capacity, excellent cycling performance and so on.[6, 7] It is widely considered as the main power source of transportation vehicles in the future.[8, 9] Due to its low cost, low toxicity and good safety performance, spinel $LiMn_2O_4$ (LMO) material is posed to be an ideal battery cathode material.[10-12] Compared with two-dimensional layered cubic rock-salt $LiCoO_2$,[13] a standard cathode material used in electronic device batteries whose structure undergoes undesirable changes that degrades its electrochemical performance,[14] especially in an overcharged state, spinel $LiMn_2O_4$ is true three-dimensional with channels capable of fast transportation of lithium ions with the relatively stable thermodynamics and preservation of its structure.[14, 15] However $LiMn_2O_4$ material has a major disadvantage, i.e., the fast fading of capacity, which is attributed to the following intrinsic chemistries: (1) Jahn–Teller effect.[16, 17] During the charge and discharge process, especially at the deep depth of lithiation, $LiMn_2O_4$ spinel phase is readily transferred into tetragonal phase $Li_2Mn_2O_4$.[11, 18] With the contraction and expansion of structural building block of MnO_6 octahedron, the spinel structure is destroyed. The structural change causes high electrical resistance, eventually resulting in the decline of electrochemical performance of the material. To maintain its structural integrity and cycle life, its capacity has to be sacrificed, i.e., the material cannot be fully intercalated/deintercalated, its discharge capacity was restricted to about 110 $mAh \cdot g^{-1}$. (2) The dissolution of manganese into the electrolyte. Mn^{3+} ion is prone to disproportionation reaction[19]:

$$2Mn^{3+} = Mn^{4+} + Mn^{2+} \quad (1)$$

The resulted Mn^{2+} ion is soluble in electrolyte and can even be electrochemical deposited on the anode,[20] resulting in significant loss of active substances and capacity during the cycling. Structural doping with other metal ions, such as Ni,[21] Co,[22] Al,[23] Ti,[24] was proved to be beneficial to improve LMO spinel structural and thermal stability.

Herein we report our synthesis and electrochemical study of intergrown $LiMn_2O_4$-$LiNi_{0.5}Mn_{1.5}O_4$ (LMO-LNMO I), which are micro-sized spheres consisted of aggregated nano-sized octahedral particles with a well-defined cubic spinel structure. In comparison, we have also synthetized spherical LMO and LNMO, and a mechanical mixture of them. The LMO-LNMO I material exhibits

several features as cathode materials: firstly, it showed an excellent rate capability with specific discharge capacities of 123, 126.5, 128.2, 127, 124 and 122 mAh·g^{-1} at 0.2 C, 0.5 C, 1 C, 2 C, 5 C and 10 C, respectively. Secondly, LNMO stabilizes the structure of LMO and is also an active material of high discharge plateau at 4.7 V,[25] resultantly enhancing the specific energy of the composite materials compared to the LMO. And thirdly, with the optimization of Mn content in LMO-LNMO I, its thermo-stability is enhanced compared to the LNMO.

Experimental

2.1. Material preparation:

The nanoscale chestnut-cupule-like MnO_2 spheres (MnO_2-S) were prepared by a solvothermal method modified from literature.[26] An aqueous solution of 20 mmol $MnSO_4$ was mixed with 8 mL concentrated sulfuric acid, then $K_2S_2O_8$ solution was quickly poured into the solution under rapid stirring. The solution was kept in a water bath of 65 ^oC undisturbed for 18 h. After filtration and washing with deionized water and ethanol, the product was dried in an oven at 100 ^oC. The standard synthetic procedures of LNMO, LMO and LMO-LNMO intergrowth (LMO-LNMO I, mole ratio of LNMO/LMO, 1/1) are as following procedures.[27] In a typical synthesis of LNMO, 15 mmol of MnO_2-S, 5 mmol of $Ni(NO_3)_2{\cdot}6H_2O$, and 10.8 mmol of $LiNO_3$ were dispersed into 20 ml ethanol. After grinded in a mortar for 30 minutes, the solution was evaporated slowly at 80 ^oC under constant stirring. The obtained precursor was firstly sintered in air at 800 ºC for 20 h, then cooled down to 600 ºC, and was maintained at this temperature for 20 h to compensate for oxygen vacancy with pyrolysis of sample before cooling to room temperature slowly. For the synthesis of LMO-LNMO I, 17.5 mmol of MnO_2-S, 2.5 mmol of $Ni(NO_3)_2{\cdot}6H_2O$, and 10.8 mmol of $LiNO_3$ were dispersed into 20 ml ethanol. Then, the following procedures were the same as that of LNMO. In the synthesis of LMO, 20 mmol of MnO_2-S, and 10.8 mmol of $LiNO_3$ were dispersed into 20 ml ethanol. Next, the following procedures were just like that of LNMO. The LMO-LNMO mixture (LMO-LNMO M) was prepared by mixing equal molar LMO and LNMO by mechanically grinding.

2.2. Material characterization:

The XRD patterns were collected on a Rigaku miniflex 600 instrument with Cu Kα radiation operated at 40 kV and 15 mA from 10º to 90º at 1º/min with a step size of 0.02º. The morphologies of samples were characterized by field emission scanning electron microscopy (SEM, HITACHI S-4800), and energy dispersive X-ray spectroscopy (EDS, OXFORD 7426) was carried out for element analysis. Transmission electron microscopy (TEM, JEOL-2100) was further used to observe the morphology and identify the structure of the as-prepared samples. Raman spectra (JOBIN Yvon Horiba Raman Spectrometer model HR800) were collected with 10 mW helium/neon laser at 532 nm excitation. The DSC/TG (STA 449 F3 Jupiter Netzsch) was used to measure the thermal stability of electrodes in 1M $LiPF_6$ salt dissolved in ethylene carbonate (EC) and dimethyl carbonate (DMC) with mass ratio of 1:1 (#301 electrolyte, Guotai Huarong, China). from 100 ºC to 300 ºC at a heating rate of 5 ºC /min. The detailed measurements were as follows. Firstly, button cell was charged to a target state, then the cell was taken apart to get electrode materials film in an Ar-filled glove box. Secondly, the film was washed several times by DMC and naturally dried. Thirdly, the electrode materials scraped from film and electrolyte were sealed together in a gold-plated stainless steel crucible in the glove box. The ratio of electrolyte to electrode materials was 1 μL of electrolyte per milligram of electrode materials.

2.3. Electrochemical measurements:

Electrochemical performances of these materials were evaluated in CR2016-type coin-cell configuration. The cathode electrode film was obtained by spreading a slurry (70 wt% active material, 20 wt% acetyleneblack, 10 wt% polyvinylidene difluoride (PVDF) binder, dispersed in N-methyl pyrrolidione (NMP) solvent) onto an aluminum foil using a high-precision coating machine.. After drying in a vacuum oven at 100 ºC overnight, the electrode was punched out and roll-pressed. The coin cells were assembled by sandwiching a porous polyethylene separator between the electrode and Li metal foil in an Ar-filled glove box. The electrolyte used was typical #301 electrolyte. The mass loading for all the cells was controlled in about 3 mg·cm^{-2}.

The cells were galvanostatically charged and discharged on a battery test system (LAND CT-2001A instrument, Wuhan, China) in the voltage range of 3.0-4.9 V at room temperature. When the rates were higher than 1 C (including 1 C), in order to overcome the polarization of the battery at high rates, a two-step charge process (constant current and constant voltage charge) was employed.[28] The specific capacity was calculated based on the total mass weight of LNMO and LMO in the electrode. The current values of various rates were calculated according to the theoretical capacity of LNMO. Take 1 C for an example, the current density value was 147 mA·g^{-1}. Cyclic voltammogram (CV) measurements were performed on a CHI 660D potentiostat (Chenghua, Shanghai, China) at a scan rate of 0.1 mV s^{-1} with potential range from 3.1 to 5.0 V. Electrochemical impedance spectra (EIS) were carried out on Solartron SI 1287 electrochemical workstation with frequency from 0.1 Hz to 100 kHz. All the tests were conducted at 25 ºC unless specified illustration.

Results and discussion

Fig. 1(a-e) shows the SEM images of manganese sources of MnO_2-S, LMO, LNMO, LMO-LNMO M and LMO-LNMO I, respectively. Our starting precursor of Mn source that micro-structured MnO_2 spheres, are quite uniform, ranging from 2 μm to 4 μm in size. Each of these MnO_2 spheres composes of many MnO_2 nano-needles radiating from its center, rendering the whole structure like a chestnut cupule. The nano-needles are well separated, with a large space between adjacent nanorods (Fig. S1), generating a much larger surface area. Thus it is a better candidate for impregnation of solutions containing other transition metal ions. After 800 ºC calcination, the morphology of spherical structure is retained and the particle size is in the range of 2–4 μm (Fig.1 c, d, and e). From the high-magnification SEM image of LMO-LNMO I shown in Fig.1 (f), it can be concluded that microspheres are further made up by nano-octahedrons, with each octahedron cross-linked by vertex or edges. Therefore, this special porous structure provides space for the infiltration of electrolyte and accommodation of the volume change to alleviate the lattice strain during the insertion-deinsertion course of lithium ion. [29, 30] SEM study does not show structural difference between LMO-LNMO M and LMO-LNMO I, but EDS elemental analysis presented in Fig. 2 clearly illustrates the difference. Fig. 2(a) shows mapping area of LMO-LNMO M and Fig. 2 (b, c) are the nickel and manganese element distributions from EDS of the selected area of LMO-LNMO M, respectively. The Nickel distribution in this sample is not as homogeneous as that of

manganese, and it is not overlapping that of manganese, which is understandable since the two components were just mechanically mixed. Fig. 2 (d, e, f) are of the sample LMO-LNMO I. The distributions of Mn and Ni are not only very uniform, but also overlapping. This demonstrates unambiguously that LMO and LNMO are formed a homogeneous material in nanoscale together rather than simply blended.

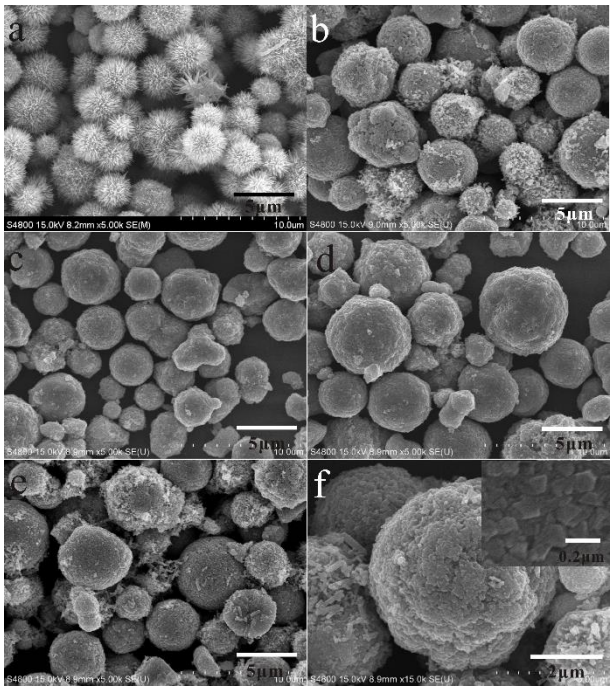

Fig. 1. SEM images of the samples (a) chestnut-like MnO_2, (b) LMO, (c) LNMO, (d) LMO-LNMO M, (e) LMO-LNMO intergrowth. (f) a magnified image of LMO-LNMO I.

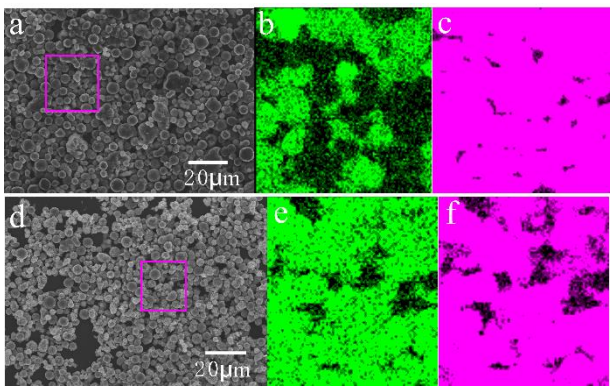

Fig. 2 (a) SEM plots of LMO-LNMO M, (b, c) EDS area mappings of Ni, Mn element in corresponding region (purple box) in SEM plots of LNMO-LMO M; (d) SEM plots of LMO-LNMO I, (e, f) EDS area mappings of Ni, Mn element in corresponding region (purple box) in SEM plots of LNMO-LMO I.

Fig. 3 shows the X-ray diffraction (XRD) patterns of the LMO, LNMO, LMO-LNMO M and LMO-LNMO I, respectively. All these samples are indexed to cubic spinel structures. There are several weak peaks (2θ = 37.335°, 43.381°and 63.024° [31]) in the LNMO which are from rock salt phase $Li_xNi_{1-x}O$/NiO. The LMO-LNMO M is a simple mixture of LMO and the LNMO, thus, several pairs of twin peaks at ca. 38, 44, 48.3, 58.3, 64.0, 67.6, 76.0, 77.0, 81.0 and 84.0° are observed. In the LMO-LNMO I, no splitting of any peak is observed, indicating that it is a single phase material. The lattice parameters, $d_{(111)}$ and the sizes of sub-grains calculated using Scherrer Equation along (111) surface are obtained from least square refinement based on a cubic structure using the PDXL2 software (Rigaku, Japan), and the results are summarized in Table 1. As we can see from the table, the crystal lattice parameters and interlayer space of (111) lattice plane for LMO are 8.2342 Å and 4.7644 Å, respectively, while for LNMO they are 8.1690 Å and 4.7224 Å. The corresponding lattice parameters of LMO-LNMO I are in between that of the LMO and LNMO. To put it simply, with Ni content increases, the lattice parameter and interlayer space of (111) shrinks. On the basis of literature, this decrease is ascribed to the concentration increase of Mn^{4+} ions in the spinel structure because Mn^{3+} ions are replaced by Ni^{2+} ions.[32] Since the percentage of Ni element in the LNMO is greater than that in LMO-LNMO I, its lattice and interlayer space of (111) are the smallest. The sub-grain sizes (Å) of the LMO, the LNMO and the LMO-LNMO I are 410.16 Å, 369.24 Å and 379.49 Å, which is accordance with the lattice parameter.

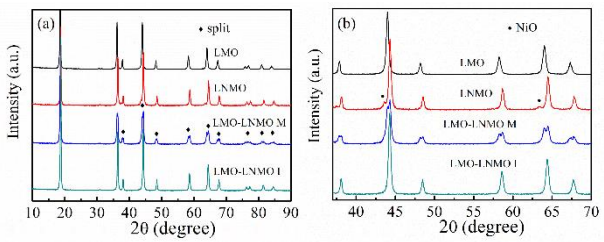

Fig. 3. XRD patterns of (a) LMO, LNMO, LMO-LNMO M and LMO-LNMO I; (b) Enlargement of 2θ = 37 to 70° range.

Table 1 The summary of the lattice parameters for all the samples (a, b, c (a = b=c), $d_{(111)}$, sizes of sub-grains.

	Lattice parameter (Å)	d (111) (Å)	Sub-grain size (Å) (111)
LMO	8.2342	4.7644	410.16
LNMO	8.1690	4.7224	369.24
LMO-LNMO I	8.1834	4.7299	379.49

The TEM characterization of the LMO-LNMO I is carried out (Fig. 4). As shown in Fig. 4(a), the LMO-LNMO I is of hollow structure, consistent with the structure of precursor. SAED pattern (Fig. 4a inset) of the whole micron-sized LMO-LNMO I sphere shows unordered diffraction spots, presenting the polycrystalline structure of the entire LMO-LNMO I sphere. Nano-sized polyhedrons in Fig. 4(b) is obtained from the magnifying micron-sized LMO-LNMO I sphere surface. A high-resolution TEM (HRTEM) image of the nano-sized polyhedron of Fig. 4(b) appears clear lattice fringes (Fig. 4(c)). The interplanar spacing lattice is 0.48 nm, which is in accordance with the d-spacing of the (111) crystal planes of the

LMO-LNMO I. SAED pattern (Fig. 4d) with the electron beam in the [110] direction corresponding to yellow area of Fig. 4(b) presents well-organized array of diffraction spots that index a typical spinel lattice structure. This means the polycrystalline LMO-LNMO I micron-sized sphere is composed of monocrystalline nano-sized polyhedrons; LMO and LNMO in LMO-LNMO I are formed a homogeneous material in unit cell scale. The ordered lattices in long-range order result in the intercalation and deintercalation of Li ion easily occurring, which is useful to improve the rate property of the cell with the material.

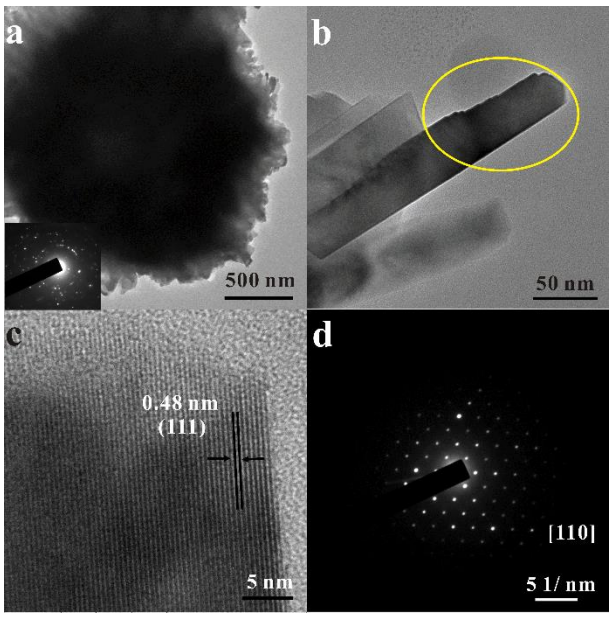

Fig. 4. TEM images of (a) the as-prepared LMO-LNMO I and (b) nano-sized polyhedra obtained from magnifying LMO-LNMO I sphere surface. (c) HRTEM image of nano-sized polyhedron (d) SAED pattern in the [110] zone of nano-sized polyhedron corresponding to yellow area of (b).

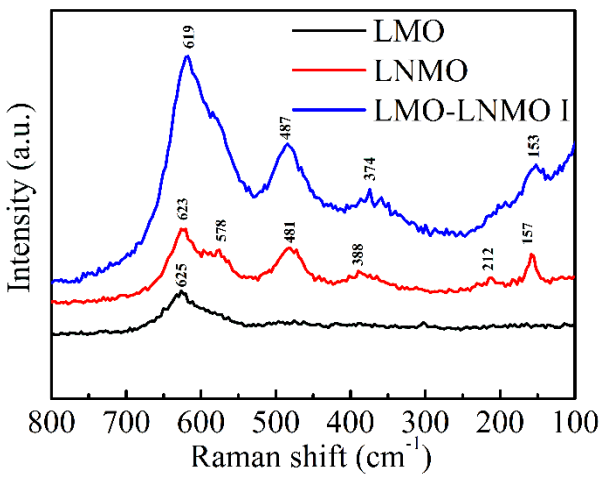

Fig. 5 Raman spectra of LMO, LNMO and LMO-LNMO I.

Raman characterization was carried out, shown in Fig. 5 to identify the structure of spinel. According to previous reports [33, 34], the strong band appeared at 623 cm^{-1} is attributed to the symmetrical Mn-O stretching vibration (A_{1g}) in MnO_6 octahedra. Peaks at around 388 and 481 cm^{-1} are related to the Ni^{2+}-O stretching mode in spinel. $T_{2g}^{(3)}$ band of the spinel is at around 575-625 cm^{-1}. The split of this $T_{2g}^{(3)}$ band is the fingerprint of $P4_332$ space group. The splitting of $T_{2g}^{(3)}$ is weak and broad hump is observed. The other characteristic peaks of $P4_332$ structure around 212, and 157 cm^{-1} are weak with some characteristic peak absent. [8, 35] All this means LNMO is a mixture of orderly $P4_332$ and disorderly Fd3m phase after annealing at 600 ºC for 20 h. According to Patoux [36], in general synthesis, the LNMO is usually of a mixture of ordered $P4_332$ phase and disordered Fd3m phase. The peaks of LMO-LNMO I are similar to LNMO with little shift of peak position. So orderly and disorderly sites of Ni and Mn in LMO-LNMO I coexist.

Cyclic voltammograms of LMO, LNMO, LMO-LNMO M and LMO-LNMO I at a scanning rate of 0.1 mV s^{-1} are shown in Fig. 6. In general, the redox peaks at around 4.1 V are ascribed to oxidation/reduction of Mn^{4+}/Mn^{3+}, while the one at 4.7 V is attributed to the redox reaction of the Ni^{4+}/Ni^{2+} couples. The peaks of LMO-LNMO M are simply additions of those of LMO and LNMO with neither shifting the peak positions nor changing relative intensities. The LMO-LNMO I exhibits distinctly differences. The peak intensity in the range of 4.0-4.3 V becomes relatively smaller and broader.

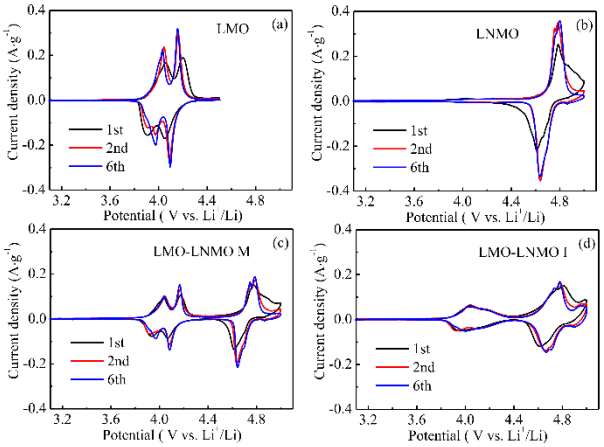

Fig. 6. Cyclic voltammogram curves (at a scan rate of 0.1mV s^{-1}) of (a) LMO, (b) LNMO, (c) LMO-LNMO M, (d) LMO-LNMO I.

The electrochemical performances of these materials at 25 ºC are given in Fig. 7. Fig. 7(c) plots their specific discharge capacities upon cycling at 1 C. The discharge capacities (here we used the fifth cycle at which their discharge capacities were stabilized) of LMO, LNMO, LMO-LNMO M, LMO-LNMO I are 111.7, 117.7, 119.7 and 128.8 mAh·g^{-1}, respectively. After 100 cycles, their specific capacities became 105.1, 113.5, 111.5 and 124.8 mAh·g^{-1}, with the specific capacity retentions of 94.1%, 96.4%, 93.2% and 96.9%, respectively. Although the content of LMO in the LMO-LNMO M up to 50% compared to LNMO and LMO, their discharge specific capacities and cycle performances are essentially the same as LNMO and better than LMO, suggesting a simple blending improves electrochemical performance of material at some extent. The LMO-LNMO I, which has better mixing of Mn and Ni ions, not only showed roughly 10% discharge capacity increase, but also the

highest capacity retention. We believe that in LMO-LNMO I, LNMO is an active material as well as a skeleton for the LMO, so that more lithium ions can take part in the insertion-deinsertion process. The charge and discharge-capacity/voltage curves of fifth cycle are plotted in Fig. 7 (a) and Fig. 7 (b). These data are consistence with the CVs plots shown in Fig. 6. Two plateaus around 4.1 V were observed for LMO, one plateau at 4.7 V for LNMO. The discharge plateaus for the LMO-LNMO M are simple addition of LMO and LNMO. The LMO-LNMO I also showed similar voltage plateau to LMO-LNMO M, but significant differences are observable: the discharge plateau around 4.7 V become larger, and the discharge plateau around 4.1 V rises to higher voltage (4.2 V). Because the platform of LMO is located at 4.1 V, so in the charge test of LMO, the cutoff voltage is set to 4.3 V. We also did the electrochemical test of LMO in the voltage range of 3.0-4.9 V as Fig. S2. It was found that there is a little increase in discharge capacity for LMO, but it is still less than that of LMO-LNMO I.

The rate capabilities of these materials are shown in Fig. 7 (d). Because of the electrochemical polarization and ohmic polarization from the restricted diffusion rate of lithium ion in spinel structure,[37] the capacity of all the samples certainly reduces at high rates. Among all these samples, LNMO showed the largest reduction in capacity at high rates, LMO-LNMO M followed LNMO, and LMO-LNMO I showed the least reduction in capacity at the same high rates, which is due to the homogeneous mixing of Ni and Mn ions in

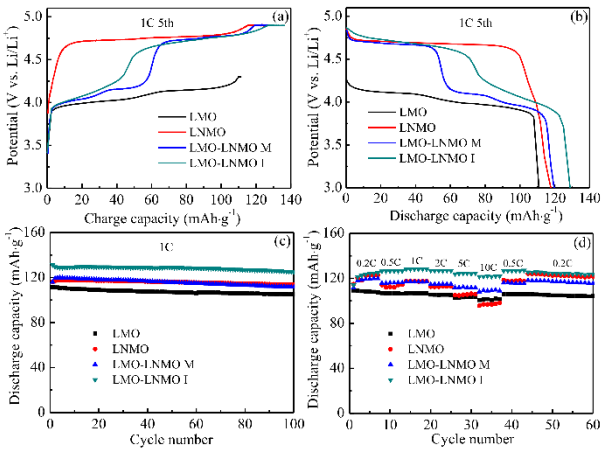

Fig. 7. Electrochemical properties of the as prepared samples (a) the 5th charge curve at 1 C; (b) the 5th discharge curve at 1 C; (c) cycle performance at 1 C; (d) rate cycling performance.

the structure. Ni ions act as structural stabilization agents to make excess lithium ion engaging in charge-discharge process; Mn ions boost the electrical conductivity of the material by making Ni sites and Mn sites more homogeneously,[25] leading to greater specific capacity at high rates. Strikingly, the discharge capacity at 1 C for the LMO-LNMO I was even higher than that at 0.5 C. Such a phenomenon has been reported by Zhou [28] and Lazarraga [38] without clear conclusion. In our opinion, this may be due to the different charging modes between 0.5 C and 1 C. In our experiment, the cells were galvanostatically charged and discharged on a battery test system between 3.0-4.9 V at room temperature at low rates. When the rates higher than 1 C (including 1 C), a two-step charge process (constant current and constant voltage charge) was employed in order to overcome the polarization of the battery at high rates. In the latter case, following the constant current charge step, the constant voltage charge process was carried out till the current reduced to one tenth of its initial constant value.

Fig. 8 shows typical cycle performances of the electrodes at a current rate of 5 C between 3.0 and 5.0 V at 55 ºC. The discharge capacity of LMO, LNMO, LMO-LNMO M, LMO-LNMO I at fifth

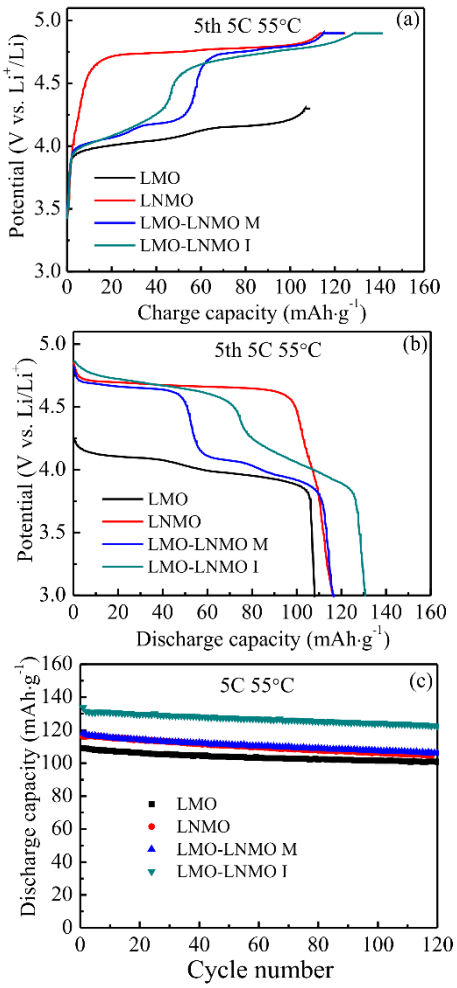

Fig. 8. Electrochemical properties of the samples at 55 ºC at 5 C: (a) the fifth charge curve, (b) the fifth discharge curve, (c) cycle performance of samples.

cycle are 108.1, 116.3, 116.6 and 130.6 mAh·g^{-1}, with a retention of 93.2%, 90.1%, 91% and 93.7% after 120 cycles, respectively. The charge platform of the LMO-LNMO I is lower than that of the LMO-LNMO M, whereas the discharge platform is higher than that of the LMO-LNMO M, indicating less ohmic polarization.[37] The LMO-LNMO M charge-discharge curves can be regarded as the simple summation of LMO and LNMO. All these suggest that Ni and Mn ions in LMO-LNMO I achieve homogeneous mixing at atomic level, making the structure more stable than LMO-LNMO M.

Electrochemical impedance spectroscopy (EIS) test was conducted to further illustrate the differences in the electrochemical polarization and ohmic polarization. All the samples were charged and discharged at 1 C by constant current and constant voltage

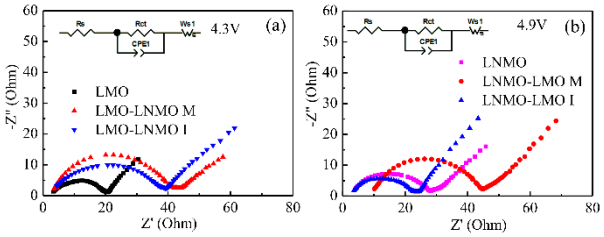

Fig. 9. EIS spectra of the samples in the frequency range between 0.1 Hz and 100 kHz at 25 ºC: (a) charged to 4.3 V, （b）charged to 4.9 V.

Table 2 The fitted results of resistances (Rs) and charge transfer resistances (Rct) for the Nyquist plots of the LMO, the LNMO, the LNMO-LMO M, and the LNMO-LMO I samples at the charged states of 4.3 V and 4.9 V.

	charge to 4.3V (Ω)		charge to 4.9V (Ω)	
	Rs	Rct	Rs	Rct
LMO	2.23	17.82		
LNMO			2.30	25.49
LMO-LNMO M	2..47	38.39	9.29	35.83
LMO-LNMO I	2.03	35.86	2.11	21.09

process. After four full cycles, the cells were charged to 4.3 V, then EIS was measured in the range from 100 kHz to 0.1 Hz. The EIS of 4.9 V charged state was achieved at similar to the above expect that cells were charged to 4.9 V at 1 C, then the potential was kept at 4.9 V until the current decreases to one tenth of its initial value. The Nyquist plots (Fig. 9 (a)) of all materials charged to 4.3 V display similar profiles: a semicircle in the high-frequency region and a linear slop in the low-frequency region. All can be fitted with same equivalent circuits as insets shown Fig. 9(a). When the materials were charged to 4.9 V, similar Nyquist plots and equivalent circuits were obtained. The fitted data was listed in Table 2. In our analysis, the Rs is assigned to electrolyte resistance, while the Rct is attributed to direct charge transfer resistance of electrode materials. [39-41] The Rct of LNMO, LMO-LNMO M and LMO-LNMO I (<40 Ω) varies substantially, $Rct_{LMO\text{-}LNMO\ M}$>$Rct_{LMO\text{-}LNMO\ I}$ >Rct_{LMO} at 4.3 V charged state and $Rct_{LMO\text{-}LNMO\ M}$> Rct_{LNMO}> $Rct_{LMO\text{-}LNMO\ I}$ at 4.9 V charged state in sequential order. This indicates that the intergrowth LMO-LNMO I reduces the barrier for the electrons transfer at the electrode−electrolyte interface. The much improved rate performance from decreasing Rct of LMO-LNMO I is attributed to its unique structure. Because of the homogeneous mixing of Ni and Mn ions at atomic level in the LMO-LNMO I, the structure became more stable and higher electrical conductive, [42] thus facilitating the insertion/deinsertion of lithium ions by the alleviation of electrochemical polarization and ohmic polarization. The Rct of LMO-LNMO M is a little bigger than that of LNMO, which maybe attributed to two phase structure of LMO-LNMO M. This is a little unfavourable to lithium ion transport.

The thermal behaviors of charged (delithiated, 4.3 V and 4.9 V) LNMO-LMO I and blend LNMO-LMO M in 301 electrolyte (1M $LiPF_6$, EC/DMC) were investigated by DSC/TG analysis as shown in Fig. 10. Pure $LiMn_2O_4$ and $LiNi_{0.5}Mn_{1.5}O_4$ spinel were also evaluated as comparisons. There are obvious different thermostability among LMO, LNMO, LMO-LNMO M and

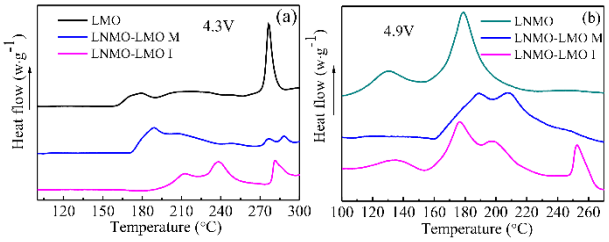

Fig. 10. DSC curves of samples in #301 electrolyte at the states charged to 4.3 V (a), and to 4.9 V (b).

LMO-LNMO I. As the battery charged to 4.3 V (Fig. 10(a)), the onset exothermic temperature for LMO is 159.4 ºC, while that of LMO-LNMO M is 171.3 ºC. The thermostability is boosted by the mixture of LMO and LNMO, but this is also inferior to LMO-LNMO I. Due to the Ni and Mn mingling at atom level, the onset exothermic temperature at 4.3 V state is back to 188.1 ºC. The total heat quantity for LMO around 160-300 ºC is 599.9 $J{\cdot}g^{-1}$, while that of LMO-LNMO I is 567.1 $J{\cdot}g^{-1}$. When the thermal stability was measured at fully delithiated state (4.9 V), the onset exothermic temperature for LMO-LNMO M is higher than that of LNMO and LMO-LNMO I, which may be attributed to a blend effect. As Tran's research,[43] after blend of 33.3% $LiNi_{0.8}Co_{0.15}Al_{0.05}O_2$ and 66.7% $LiMn_2O_4$, thermal stability of the blending material is improved tremendously than $LiNi_{0.8}Co_{0.15}Al_{0.05}O_2$ and $LiMn_2O_4$ monomer. The LNMO-LMO I is a little lower in onset exothermic temperature, but has the lowest reaction heat flow of 518.9 J g^{-1} in the temperature range of 100-280 ºC. For LNMO-LMO M and LNMO, the reaction heat flow is nearly the same, 698.6 J g^{-1} and 689.6 J g^{-1}, respectively. These results suggest that the LNMO-LMO I structure has the stable structure compared to LMO, LNMO and LNMO-LMO M.

Conclusion

In this work，the porous micro-sized sphere of intergrown LMO-LNMO I particles are successfully synthesized *via* an impregnation method based on highly reactive chestnut-like MnO_2 spheres as the manganese sources and structural template. The LMO-LNMO I is comprised of nano-sized octahedron with good crystalline in a particle size range of 2-4 μm. In this special structure, the LNMO is worked as a skeleton to stabilize the structure of LMO, ensuring more lithium ions in LMO participate in charge-discharge process along with LNMO. As a result, LMO-LNMO presents a discharge specific capacity of 130 mAh·g at 1 C at 25 ºC, with a capacity retention of 96.2% after 100 cycles. It also shows an excellent performance at high temperature and high rate. It can deliver a discharge capacity of 131 $mAh{\cdot}g^{-1}$, with capacity retention of 95% after 100 cycles at 5 C at 55 ºC. Meanwhile, with the Mn content improving and better Ni/Mn ions mixing in the LMO-LNMO I than LNMO and LMO-LNMO M, the thermostability of LNMO-LMO I is much improved compared with LNMO. The high capacity, excellent rate capability, remarkable cycling stability at room and elevated temperature of the LMO-LNMO I make it a promising cathode material for lithium ion batteries.

Acknowledgements

The authors gratefully acknowledge the financial supports from the National High Technology Research and

Development Program of China (2012AA110204), Key Project of Science and Technology of Fujian Province (2013H6022) and Science and Technology Bureau of Xiamen (Grant No. 3502Z20133004). Jiyang Li expresses their special thanks to National Found for Fostering Talents of Basic Science (J1310024). The authors also wish to express their thanks to Drs. Dong Sun and Binbin Xu for their valuable suggestions.

Notes and references

State Key Lab of Physical Chemistry of Solid Surfaces, Collaborative Innovation Center of Chemistry for Energy Materials, College of Chemistry and Chemical Engineering, Xiamen University, Xiamen, Fujian, 361005, China. E-mail: jbzhao@xmu.edu.cn.; Fax: +86-592-2186935; Tel: +86-592-2186935.

†Electronic Supplementary Information (ESI) available. See DOI: 10.1039/b000000x/

1. D. Liu, J. Trottier, P. Charest, J. Fréchette, A. Guerfi, A. Mauger, C. M. Julien and K. Zaghib, *J. Power Sources*, 2012, **204**, 127-132.
2. S. Yang, J. Chen, Y. Liu and B. Yi, *J. Mater Chem. A*, 2014, **2**, 9322-9330.
3. J. Yang, F. Cheng, X. Zhang, H. Gao, Z. Tao and J. Chen, *J. Mater Chem. A*, 2014, **2**, 1636-1640.
4. X. Wu, S. Wang, X. Lin, G. Zhong, Z. Gong and Y. Yang, *J. Mater Chem. A*, 2014, **2**, 1006-1013.
5. J. Wang, W. Lin, B. Wu and J. Zhao, *Electrochim. Acta*, 2014, **145**, 245-253.
6. Z. Yang, J. Zhang, M. C. W. Kintner-Meyer, X. Lu, D. Choi, J. P. Lemmon and J. Liu, *Chem. Rev.*, 2011, **111**, 3577-3613.
7. J. Wang, W. Lin, B. Wu and J. Zhao, *J. Mater Chem. A*, 2014, **2**, 16434-16442.
8. G. B. Zhong, Y. Y. Wang, X. J. Zhao, Q. S. Wang, Y. Yu and C. H. Chen, *J. Power Sources*, 2012, **216**, 368-375.
9. G.N. Zhu, L. Chen, Y.G. Wang, C.X. Wang, R.C. Che and Y.Y. Xia, *Adv. Funct. Mater*, 2013, **23**, 640-647.
10. Y.L. Ding, J. Xie, G.S. Cao, T.J. Zhu, H.M. Yu and X.B. Zhao, *Adv. Funct. Mater*, 2011, **21**, 348-355.
11. M.J. Lee, S. Lee, P. Oh, Y. Kim and J. Cho, *Nano Lett.*, 2014.
12. D. Tang, Y. Sun, Z. Yang, L. Ben, L. Gu and X. Huang, *Chem. Mater.*, 2014, **26**, 3535-3543.
13. Y. Koyama, H. Arai, I. Tanaka, Y. Uchimoto and Z. Ogumi, *J. Mater Chem. A*, 2014, **2**, 11235-11245.
14. H.M. Cheng, F.M. Wang, J. P. Chu, R. Santhanam, J. Rick and S.C. Lo, *J. Phys. Chem. C*, 2012, **116**, 7629-7637.
15. S. Lee, Y. Cho, H.K. Song, K. T. Lee and J. Cho, *Angew. Chem.*, 2012, **124**, 8878-8882.
16. T.F. Yi, Y. Xie, Y.R. Zhu, R.S. Zhu and M.F. Ye, *J. Power Sources*, 2012, **211**, 59-65.
17. H.W. Lee, P. Muralidharan, R. Ruffo, C. M. Mari, Y. Cui and D. K. Kim, *Nano Lett.*, 2010, **10**, 3852-3856.
18. Y. Wu, Z. Wen, H. Feng and J. Li, *Small*, 2012, **8**, 858-862.
19. S. Brutti, G. Greco, P. Reale and S. Panero, *Electrochim. Acta*, 2013, **106**, 483-493.
20. J.-H. Kim, N. P. W. Pieczonka, Z. Li, Y. Wu, S. Harris and B. R. Powell, *Electrochim. Acta*, 2013, **90**, 556-562.
21. Y. J. Wei, L. Y. Yan, C. Z. Wang, X. G. Xu, F. Wu and G. Chen, *J. Phys. Chem. B*, 2004, **108**, 18547-18551.
22. S. Mandal, R. M. Rojas, J. M. Amarilla, P. Calle, N. V. Kosova, V. F. Anufrienko and J. M. Rojo, *Chem. Mater.*, 2002, **14**, 1598-1605.
23. Y. L. Ding, J. Xie, G. S. Cao, T. J. Zhu, H. M. Yu and X. B. Zhao, *J. Phys. Chem. C*, 2011, **115**, 9821-9825.
24. S. Wang, J. Yang, X. Wu, Y. Li, Z. Gong, W. Wen, M. Lin, J. Yang and Y. Yang, *J. Power Sources*, 2014, **245**, 570-578.
25. J. Xiao, X. Chen, P. V. Sushko, M. L. Sushko, L. Kovarik, J. Feng, Z. Deng, J. Zheng, G. L. Graff, Z. Nie, D. Choi, J. Liu, J.-G. Zhang and M. S. Whittingham, *Adv. Mater.*, 2012, **24**, 2109-2116.
26. H.E. Wang and D. Qian, *Mater. Chem. Phys.*, 2008, **109**, 399-403.
27. X. Zhu, X. Li, Y. Zhu, S. Jin, Y. Wang and Y. Qian, *Electrochim. Acta*, 2014, **121**, 253-257.
28. L. Zhou, D. Zhao and X. Lou, *Angew. Chem.*, 2012, **124**, 243-245.
29. S. Liang, J. Yi and A. Pan, *Int. J. Electrochem. Sci*, 2013, **8**, 6535-6543.
30. X. W. Lou, L. A. Archer and Z. Yang, *Adv. Mater.*, 2008, **20**, 3987-4019.
31. J. Song, D. W. Shin, Y. Lu, C. D. Amos, A. Manthiram and J. B. Goodenough, *Chem. Mater.*, 2012, **24**, 3101-3109.
32. Q. Zhong, A. Bonakdarpour, M. Zhang, Y. Gao and J. R. Dahn, *J. Electrochem. Soc.*, 1997, **144**, 205-213.
33. C. M. Julien and M. Massot, *Mater. Sci. Eng. B*, 2003, **97**, 217-230.
34. S. H. Oh, K. Y. Chung, S. H. Jeon, C. S. Kim, W. I. Cho and B. W. Cho, *J. Alloys Compd.*, 2009, **469**, 244-250.
35. G. B. Zhong, Y. Y. Wang, Y. Q. Yu and C. H. Chen, *J. Power Sources*, 2012, **205**, 385-393.
36. S. Patoux, L. Daniel, C. Bourbon, H. Lignier, C. Pagano, F. Le Cras, S. Jouanneau and S. Martinet, *J. Power Sources*, 2009, **189**, 344-352.
37. O. Sha, Z. Tang, S. Wang, W. Yuan, Z. Qiao, Q. Xu and L. Ma, *Electrochim. Acta*, 2012, **77**, 250-255.
38. M. G. Lazarraga, L. Pascual, H. Gadjov, D. Kovacheva, K. Petrov, J. M. Amarilla, R. M. Rojas, M. A. Martin-Luengo and J. M. Rojo, *J. Mater Chem.*, 2004, **14**, 1640-1647.
39. L. J. Xi, H.E. Wang, Z. G. Lu, S. L. Yang, R. G. Ma, J. Q. Deng and C. Y. Chung, *J. Power Sources*, 2012, **198**, 251-257.
40. J. Chong, S. Xun, X. Song, G. Liu and V. S. Battaglia, *Nano Energy*, 2013, **2**, 283-293.
41. J. Lu, Q. Peng, W. Wang, C. Nan, L. Li and Y. Li, *J. Am. Chem. Soc.*, 2013, **135**, 1649-1652.
42. M. Kunduraci, J. F. Al-Sharab and G. G. Amatucci, *Chem. Mater.*, 2006, **18**, 3585-3592.
43. H. Y. Tran, C. Täubert, M. Fleischhammer, P. Axmann, L. Küppers and M. Wohlfahrt-Mehrens, *J. Electrochem. Soc.*, 2011, **158**, A556-A561.